

A model of membrane deformations driven by a surface pH gradient

Toni V. Mendes,^{1,2} Jonas Ranft,³ and H el ene Berthoumieux^{2,4}

¹⁾Laboratoire Ondes et Mati ere d'Aquitaine, Universit e de Bordeaux, Unit e Mixte de Recherche 5798, CNRS, F-33400 Talence, France

²⁾Sorbonne Universit e, CNRS, Laboratoire de Physique Th eorique de la Mati ere Condens ee (LPTMC, UMR 7600), F-75005 Paris, France

³⁾Institut de Biologie de l'ENS, Ecole Normale Sup erieure, CNRS, Inserm, Universit e PSL, 46 rue d'Ulm, F-75005 Paris, France

⁴⁾Fachbereich Physik, Freie Universit at Berlin, Arnimallee 14, Berlin, 14195, Germany

Many cellular organelles are membrane-bound structures with complex membrane composition and shape. Their shapes have been observed to depend on the metabolic state of the organelle, and the mechanisms that couple biochemical pathways and membrane shape are still actively investigated. Here, we study a model coupling inhomogeneities in the lipid composition and membrane geometry via a generalized Helfrich free energy. We derive the resulting stress tensor, the Green's function for a tubular membrane and compute the phase diagram of the induced deformations. We then apply this model to study the deformation of mitochondria cristae described as membrane tubes supporting a pH gradient at its surface. This gradient in turn controls the lipid composition of the membrane via the protonation/deprotonation of cardiolipins, which are acid-based lipids known to be crucial for mitochondria shape and functioning. Our model predicts the appearance of tube deformations resembling the observed shape changes of cristae when submitted to a proton gradient.

I. INTRODUCTION

Lipid membranes are fundamental components of cells as they compartmentalize space. Notably, many organelles important for cellular function such as the endoplasmic reticulum, the Golgi apparatus, or mitochondria are membrane-enclosed structures. For this last case, the lipid membrane also takes part in biochemical processes that it encloses by facilitating the 2D diffusion of reactants (protons)¹. Physical descriptions of membranes as two-dimensional sheets with a mechanical energy given by the Helfrich model², which in addition to surface tension assumes a quadratic dependence of the energy on the intrinsic mean curvature of the surface, have been very successful in capturing the rich variety of shapes observed for *in vitro* systems³. Since Helfrich's seminal work, many extensions to his model were proposed to take into account internal degrees of freedom of the membrane such as variations of membrane mass density and/or composition by way of introducing additional terms in the Hamiltonian^{4,5}. Beyond scalar degrees of freedom, vectorial fields such as a local lipid tilt can be considered with this approach^{6,7}.

At a first glance, Gaussian Hamiltonians for membrane mechanics are simple functionals that can be constructed using a Landau-Ginzburg expansion of the surface energy. However, obtaining the equilibrium shape of the surface by a straightforward minimization of the Hamiltonian can become very tricky, and sometimes proves impractical. The variational calculus expressed in terms of differential geometry (characterizing the surface by its intrinsic basis, metric, curvature tensors etc.) becomes quickly complex and cumbersome. Illustrating these difficulties, the "shape equation" associated with the Helfrich Hamiltonian was derived more than ten years after the introduction of the Helfrich model⁸. In an important de-

velopment, Guven and coworkers made the minimization process much more elegant and easy by the introduction of a constrained functional⁹⁻¹¹. In short, the geometrical relations imposed by surface continuity are enforced using Lagrange multipliers, one of which being the surface stress tensor¹². The general identification of the stress tensor for any Helfrich-type model and arbitrary geometry now makes the exploration of resulting membrane shapes considerably simpler.

Besides lipid membranes, the cell cortex is another fundamental cellular surface. Remarkably, a stochastic chemico-mechanical energy conversion driven by ATP hydrolysis can lead to a local increase of its mechanical tension and internal torque^{13,14}. From a more general point of view, the mechanics of these out-of-equilibrium surfaces can be described via constitutive relations for tensions, torques and surface chemical fluxes including so-called active terms that would not exist in passive surfaces^{13,14}. This coupling between active agent concentration and surface mechanics gives rise to the spontaneous formation of nontrivial shapes¹⁵. Lipid vesicles can also deform or divide in response to chemical stimuli and the development of such minimal models for biological self-reproduction has gained attention in last decades¹⁶. In particular, pH variation was shown to affect the bending modulus of bilayers and to generate tubular invaginations¹⁷.

Proton diffusion along biological membranes is essential for *in cellulo* energy production, and the role of the membrane composition in this mechanism is a domain of active research^{18,19}. In mitochondria, the shape of the inner membrane invaginations (cristae) enclosing ATP production varies with rate of ATP synthesis which itself is coupled to a flux of protons diffusing on the membrane^{20,21}. Inspired by this observation, a model of a tubular membrane described by a phenomenological pH-

dependent Helfrich Hamiltonian and submitted to a spatially modulated proton flux was proposed²². It could reproduce some qualitative observations of the coupling between cristae shape and metabolic state of the organelle.

In this work, we study the shapes of inhomogeneous membranes that are composed of two lipids which ratio is driven by an external surface chemical flux. We then apply this model to describe mitochondria cristae shapes as a function of a varying proton flux. The work is organized as follows. We start by introducing an Helfrich Hamiltonian which, in addition to the geometrical terms, includes a contribution related to the lipid composition and mass density based on a Landau-Ginzburg approach. In particular we take into account coupling terms between the local curvature and these physical parameters. We then derive the stress tensor of this model in an intrinsic surface reference frame. We consider the case of a cylindrical geometry and compute the Green's function of the system, defined as the expression for the deformation field for a punctual perturbation in the membrane composition. The richness of the phase diagram suggests that such a model could be relevant to describe *in vivo* membranes. We finally apply our formalism to model the shape of the mitochondrial membrane invaginations, the cristae, as finite tubes driven by a proton flux of varying intensity. We show that this model reproduces qualitatively the shape observed *in vivo* and the shape change between 'active' mitochondria (state III) and mitochondria in a rest state (state IV)²⁰. We conclude with a summary and a discussion of our results.

II. INHOMOGENEOUS MEMBRANES: LANDAU-GINZBURG HAMILTONIAN AND RESULTING SHAPES

A. Helfrich model with composition-dependent free energy

We consider a curved surface, the Cartesian coordinates of which are given by the 3D vector field $\mathbf{X}(s_1, s_2)$. The surface is parametrized by two generalized coordinates s_1, s_2 . One can then obtain the local intrinsic basis of \mathbf{X} , $(\mathbf{e}_1, \mathbf{e}_2)$, defined as $\mathbf{e}_a = \partial_a \mathbf{X}$, ($a = 1, 2$), and the normal vector $\mathbf{n} = \mathbf{e}_1 \times \mathbf{e}_2 / |\mathbf{e}_1 \times \mathbf{e}_2|$, a vector of unit length perpendicular to the surface, see Fig. 1a. We can furthermore define the two fundamental forms of the surface, i.e. the metric tensor $g_{ab} = \mathbf{e}_a \cdot \mathbf{e}_b$ and the curvature tensor $K_{ab} = \mathbf{e}_a \cdot \partial_b \mathbf{n}$. The surface element dA is equal to $dA = \sqrt{g} ds_1 ds_2$, where $g = \det g_{ab}$ is the determinant of the metric tensor. For the tensorial calculations below, we remind the Einstein summation convention and the passage from covariant to contravariant coordinates, such that $T_b^a = T_{bk} g^{ka} = \sum_{k=1,2} T_{bk} g^{ka}$, with $g^{ab} = g_{ab}^{-1}$, for \mathbf{T} a tensor of rank 2.

Let us now consider a membrane composed of two lipids L_1 and L_2 linked by a chemical reaction $L_1 \rightleftharpoons L_2$, with respective surface mass densities $\rho_{L_1}(s_1, s_2)$ and

$\rho_{L_2}(s_1, s_2)$. We introduce two scalar fields to describe the internal degrees of freedom of this inhomogeneous membrane: the mass density $\rho(s_1, s_2) = \rho_{L_1} + \rho_{L_2}$ of the two lipids and the relative mass fraction $\phi(s_1, s_2) = \rho_{L_2}/\rho$ of the lipid L_2 , which gives the local lipid composition. We then define a homogeneous reference state (ϕ_0, ρ_0) for the system. In this state, the mass density ρ_0 and the composition ϕ_0 are constant along the surface. Finally, we characterize inhomogeneous states of the membrane using

$$r(s_1, s_2) = \frac{\rho(s_1, s_2) - \rho_0}{\rho_0}, \quad \psi(s_1, s_2) = \frac{\phi(s_1, s_2) - \phi_0}{\phi_0} \quad (1)$$

where $r(s_1, s_2)$ and $\psi(s_1, s_2)$ denote the deviations from the reference state density and composition, respectively. Using the fields introduced above, we propose the following Hamiltonian to govern the equilibrium shape of such an inhomogeneous membrane:

$$H = \int_{\Omega} dA \left[\frac{1}{2} \kappa (C - C_0)^2 + \sigma_0 + \sigma_1 r \psi + \alpha_1 \psi (C - C_{eq}) + \frac{\alpha_2}{2} \psi^2 + \beta_1 r (C - C_{eq}) + \frac{\beta_2}{2} r^2 \right]. \quad (2)$$

This functional includes the standard Helfrich energy density in the first two terms, with $C(s_1, s_2) = \text{Tr}(K_a^b)$, being the mean local curvature of the surface, C_0 and $C_{eq}(s_1, s_2)$ are respectively the spontaneous and the equilibrium curvature of the reference state ($\psi=0, r=0$), κ the surface bending rigidity, and σ_0 the membrane surface tension. The shape of the reference state is obtained by minimizing the classical Helfrich Hamiltonian. Note that the Gaussian bending rigidity has been neglected here for simplicity.

The subsequent terms were obtained by following a Landau-Ginzburg approach to take into account the effect of a variation in the membrane composition on its shape. They include a self-energy contribution, $\int (\alpha_2 \psi^2/2 + \beta_2 r^2/2 + \sigma_1 r \psi) dA$, depending only on the chemical state of the membrane and of phenomenological parameters α_2, β_2 , and σ_1 ; and terms that couple the geometry, *via* the curvature, to the density, $\beta_1 r (C - C_{eq})$, or to the compositional inhomogeneity, $\alpha_1 \psi (C - C_{eq})$. These terms can originate when one considers lipids L_1 and L_2 of different shapes (see Fig. 1 for an illustration of such shapes). The strengths of these couplings to the membrane shape are captured by the parameters β_1 and α_1 . Note that $\alpha_2, \beta_2 > 0$ for the energy to be well-defined, whereas α_1, σ_1 , and β_1 can be either positive or negative.

B. Stress tensor, force balance, and the shape equation

The stationary shape of a membrane described by a Helfrich-like Hamiltonian can be obtained from the shape equation, i.e., the force balance along the surface projected on the normal vector \mathbf{n} (see Fig. (1)). Following

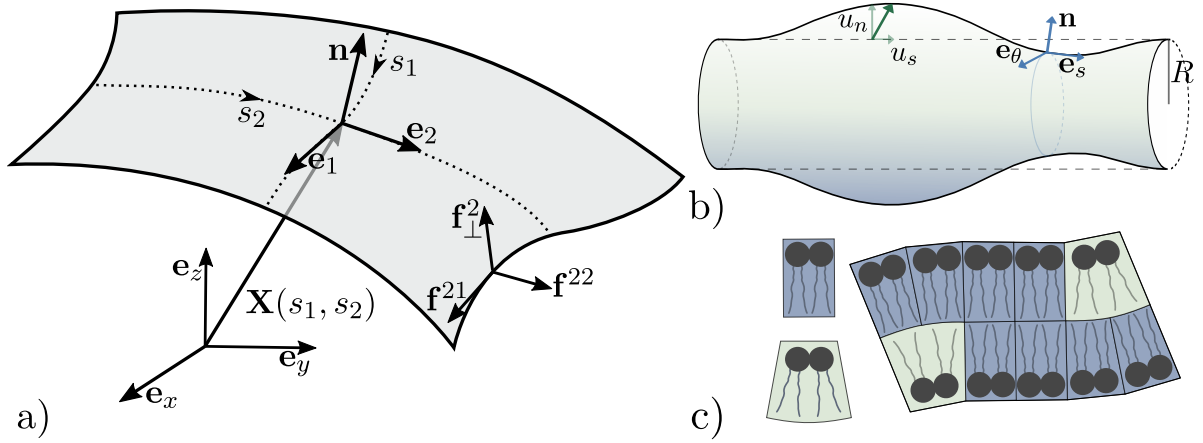


FIG. 1. (a) Representation of a 3D surface, a local basis ($\mathbf{e}_1, \mathbf{e}_2$), a normal vector \mathbf{n} and the stress tensor showing the 3 possible stresses one can apply on a surface cut. b) Cylinder of radius R deformed by the field $\mathbf{u} = u_n \mathbf{n} + u_s \mathbf{e}_s$. c) Sketch of a cylindrical lipid (blue) and a conic (green) lipid and of a membrane with a curvature induced by composition inhomogeneity.

Guen and coworkers^{9–11}, we start with the derivation

of the membrane stress tensor by introducing the constrained Hamiltonian

$$\begin{aligned}
 H_c = H &+ \int_{\Omega} \lambda^{ab} (g_{ab} - \mathbf{e}_a \cdot \mathbf{e}_b) dA + \int_{\Omega} \Lambda^{ab} (K_{ab} - \mathbf{e}_a \cdot \partial_b \mathbf{n}) dA + \int_{\Omega} \mathbf{f}^a \cdot (\mathbf{e}_a - \partial_a \mathbf{X}) dA \\
 &+ \int_{\Omega} \lambda_{\perp}^a (\mathbf{e}_a \cdot \mathbf{n}) dA + \int_{\Omega} \lambda_n (\mathbf{n}^2 - 1) dA.
 \end{aligned} \tag{3}$$

Here, the Lagrange multipliers λ^{ab} , Λ^{ab} , \mathbf{f}^a , λ_{\perp}^a , and λ_n have been introduced to enforce the local definitions of the metric, the curvature tensor, the intrinsic basis, and the normal vector, respectively.

Previously, the Lagrange multiplier \mathbf{f}^a has been identified as the stress tensor of the system^{9–11}. Its expression can be obtained via the variational minimization of H_c with respect to the now 12 independent functions \mathbf{X} , \mathbf{e}_a , \mathbf{n} , K_{ab} , g_{ab} , and r . Note that we do not minimize with respect to the composition field ψ , which we consider to be an input of our model. We eventually obtain the following set of equations:

$$\mathbf{X} : 0 = \nabla_a \mathbf{f}^a \tag{4}$$

$$\mathbf{e}_a : 0 = -\mathbf{f}^a + (\Lambda^{ac} K_c^b + 2\lambda^{ab}) \mathbf{e}_b - \lambda_{\perp}^a \mathbf{n} \tag{5}$$

$$\mathbf{n} : 0 = (\nabla_b \Lambda^{ab} + \lambda_{\perp}^a) \mathbf{e}_a + (2\lambda_n - \Lambda^{ab} K_{ab}) \mathbf{n} \tag{6}$$

$$K_{ab} : 0 = \Lambda_{ab} + \mathcal{H}^{ab} \tag{7}$$

$$g_{ab} : 0 = \lambda^{ab} - \frac{1}{2} T^{ab} \tag{8}$$

$$r : 0 = \beta_2 r + \frac{\beta_1}{R^2} (\mathcal{C} - \mathcal{C}_{eq}) + \sigma_1 \psi. \tag{9}$$

Here, \mathcal{H}^{ab} and T^{ab} are the functional derivatives of the Hamiltonian density \mathcal{H} (defined according to $H = \int dA \mathcal{H}(s_1, s_2)$) with respect to the two fundamental

forms K_{ab} and g_{ab} :

$$\mathcal{H}^{ab} = \frac{\delta \mathcal{H}}{\delta K_{ab}} \tag{10}$$

$$T^{ab} = -\frac{2}{\sqrt{g}} \frac{\delta \sqrt{g} \mathcal{H}}{\delta g_{ab}}. \tag{11}$$

and ∇_a is the covariant derivative. When \mathcal{H} depends explicitly only on the local mean curvature \mathcal{C} , these derivatives can be expressed as

$$T^{ab} = -\mathcal{H} g^{ab} + 2 \frac{\partial \mathcal{H}}{\partial \mathcal{C}} K^{ab}, \tag{12}$$

$$\mathcal{H}^{ab} = \frac{\partial \mathcal{H}}{\partial \mathcal{C}} g^{ab}. \tag{13}$$

From Eqs. (4-9), one can obtain the membrane stress tensor \mathbf{f}^a

$$\mathbf{f}^a = \left(-\mathcal{H} g^{ab} - K^{ab} \frac{\partial \mathcal{H}}{\partial \mathcal{C}} \right) \mathbf{e}_b - \nabla_b \left(\frac{\partial \mathcal{H}}{\partial \mathcal{C}} g^{ab} \right) \mathbf{n}, \tag{14}$$

which expressed in the intrinsic basis is a 3×2 matrix.

With this definition, in the absence of external forces, the force balance equations read,

$$\nabla_a f_{\perp}^a - K_{ab} f^{ab} = 0, \tag{15}$$

$$\nabla_a f^{ab} + K_a^b f_{\perp}^a = 0, \tag{16}$$

where $f^{ab} = (T^{ab} - \mathcal{H}^{ac}K_c^b)$, $f_{\perp}^a = -(\nabla_b \mathcal{H}^{ab})$, the tangential and normal components of the stress tensor such that $\mathbf{f}^a = f^{ab}\mathbf{e}_b + f_{\perp}^a\mathbf{n}$ (see Eq. (14)). Eq. (15) corresponds to the force balance along the tangential directions. The force balance along the normal direction, given in Eq. (16), is generally referred to as the shape equation.

C. Green's function for a tubular membrane and phase diagram of deformed shapes

We now apply this framework to a cylindrical geometry and consider an infinite cylindrical membrane of radius R . We consider the reference state to be a cylinder with $\psi_0 = 0$, $r_0 = 0$. For vanishing inhomogeneities, the system is described by the standard Helfrich model. Note that if $\psi = 0$ and $\mathcal{C} = \mathcal{C}_{eq}$, then $r = 0$ follows from equation Eq. 9. Using Eqs. (12-14), we derive the tangential stress tensor for the reference state. We express it in the intrinsic coordinates: $\theta = s_1$, the revolution angle, and $s = s_2$, the arclength, associated with the intrinsic basis ($\mathbf{e}_{\theta}, \mathbf{e}_s, \mathbf{n}$). Note that this coordinate system coincides with the cylindrical basis for the undeformed state. It reads

$$f_0^{ab} = \begin{pmatrix} \frac{\kappa(1-X^2)-2\sigma_0 R^2}{2R^4} & 0 \\ 0 & -\frac{\kappa(1-X)^2}{2R^2} - \sigma_0 \end{pmatrix}, \quad (17)$$

where we have introduced the dimensionless parameter

$$X = RC_0. \quad (18)$$

The normal part of the stress tensor, ($f_{\perp 0}^{\theta}, f_{\perp 0}^s$) vanishes.

The force balance in the direction \mathbf{e}_{θ} , Eq. (15), vanishes for symmetry reasons. The remaining force balance, along the normal direction, for the undeformed cylinder,

Eq. (16), reads

$$\frac{1}{2} \frac{\kappa}{R^3} (1 - X^2) - \frac{\sigma_0}{R} = 0. \quad (19)$$

Assuming positive values for the tension σ_0 , the domain of stable solutions for Eq. (19) is $X \in]-1, 1[$ and one eventually obtains the following solution for the equilibrium radius R in the reference state,

$$R = \frac{1}{C_{eq}} = \frac{1}{\sqrt{\mathcal{C}_0^2 + 2\sigma_0/\kappa}}, \quad (20)$$

where we have used the knowledge that the curvature of a cylinder (here C_{eq}) is $1/R$. Note the curvature at the equilibrium equals the spontaneous curvature only for vanishing tension. We use this relation to express the bending rigidity κ in terms of R , σ_0 , and X in the following.

We next derive the shape of a deformed cylinder in response to a ring-like perturbation of the composition obeying the rotational symmetry of the cylinder, $\psi(\theta, s) = \psi(s)$, with $\psi(s) = \delta\psi\delta(s)$, where $\delta\psi$ is a magnitude and $\delta(s)$ a Dirac delta for the surface coordinate s , see Fig. 1b. To describe the deformations induced by the perturbation, we introduce the deformation field $\mathbf{u}(s) = u_n(s)\mathbf{n} + u_s(s)\mathbf{e}_s$ with radial and tangential components $u_n(s)$ and $u_s(s)$, respectively (see Fig. 1b), where s is now the arclength associated with the deformed shape. The differential geometry elements associated with the deformed tube, i.e., the intrinsic basis $\mathbf{e}_{\theta}, \mathbf{e}_s, \mathbf{n}$, as well as the metric and mean curvature of the surface, are given in the Appendix A. We derive them up to first order in the response fields, i.e., the deformation fields (u_n, u_s) and the density inhomogeneity r , which are assumed to be small - i.e., $u_n/R, u_s/R$ and $r \ll 1$.

The surface stress tensor in the deformed state writes $f = f_0 + f_1$ and f_1^{ab} can be decomposed into a mechanical part that depends on (u_n, u_s) and a chemical part that is a function of (r, ψ) such that $f_1^{ab} = f_{1,M}^{ab} + f_{1,C}^{ab}$, where

$$f_{1,M}^{ab} = \begin{pmatrix} -\frac{2\sigma_0}{R^3(1-X^2)}(u_n + XR^2u_n'') & 0 \\ 0 & \frac{2\sigma_0}{R(1+X)}u_n + \frac{4\sigma_0}{1+X}u_s' \end{pmatrix}, \quad (21)$$

$$f_{1,C}^{ab} = \begin{pmatrix} \frac{1}{R^3}(\beta_1 r + \sigma_1 \psi) & 0 \\ 0 & 0 \end{pmatrix}. \quad (22)$$

The same decomposition can be applied to the normal part of the stress tensor, $f_{\perp}^a = f_{\perp 1,M}^a + f_{\perp 1,C}^a$, with

$$f_{\perp 1,M}^a = \left(0, \frac{2\sigma_0}{1-X^2}(u_n' + R^2u_n''') \right) \quad (23)$$

$$f_{\perp 1,C}^a = (0, -\beta_1 r' - \alpha_1 \psi'). \quad (24)$$

As can be seen from Eqs. (21-24), the coupling of the membrane curvature and the internal degrees of freedom r and ψ leads to extra lateral tensions and extra bending forces proportional to the coupling coefficients. Using the expression of the stress tensor and the force balance along \mathbf{e}_s and \mathbf{n} , using $r(s) = -\frac{\beta_1}{\beta_2 R^2}(\mathcal{C}(s) - \frac{1}{R}) - \frac{\sigma_1}{\beta_2}\psi(s)$ according to Eq. (9) in the force balance along \mathbf{n} , one gets the following shape equation for the system:

$$\frac{\beta_1^2}{\beta_2 R^2} (u_n + 2R^2 u_n'' + R^4 u_n'''') - \frac{2\sigma_0}{1-X^2} (u_n + 2XR^2 u_n'' + R^4 u_n'''') = \left(\alpha_1 - \sigma_1 \frac{\beta_1}{\beta_2} \right) (\psi + R^2 \psi''). \quad (25)$$

The left-hand part is the differential equation controlling the normal deformation field u_n , the right-hand part corresponds to the source term in ψ . One sees here the predominant role played by the coupling between density and curvature proportional to β_1 . The prefactor of the higher-order derivative term in u_n'''' is equal to $(\beta_1^2/\beta_2 - \kappa)R^2$.

For a non-vanishing coupling ($\beta_1 \neq 0$), one can define an effective bending constant based on the prefactor of u_n'''' in the shape equation (25). Let us now define the Green's function of the system, $G_\perp(s)$, according to $u_n(s) = \int ds' G_\perp(s-s') \psi(s')$. Performing a Fourier transform of Eq. (25), one gets

$$\frac{\tilde{G}_\perp(q)}{R} = \frac{\delta\psi}{2\sqrt{2\pi}} \frac{Z(1-X^2)(R^2 q^2 - 1)}{[Y(1-X^2) - 1]R^4 q^4 - 2[Y(1-X^2) - X]R^2 q^2 + Y(1-X^2) - 1}, \quad (26)$$

where we have furthermore introduced the two additional dimensionless parameters

$$Y = \frac{\beta_1^2}{2\sigma_0\beta_2 R^2} \quad \text{and} \quad Z = \frac{1}{R\sigma_0} \left(\alpha_1 - \sigma_1 \frac{\beta_1}{\beta_2} \right). \quad (27)$$

Note that we used the convention of the Fourier transform $\tilde{u}(q) = 1/\sqrt{2\pi} \int ds e^{iqs} u(s)$.

The Green's function is a function of the three dimensionless parameters X , Y , and Z that obey $-1 < X < 1$, $Y \geq 0$ and Z unbounded. While X (defined in Eq. (17)) depends only on the geometric parameters, Y and Z are non-trivial functions of the parameters introduced in the Landau-Ginzburg expansion of the Hamiltonian given in Eq. (2). Z determines the amplitude and sign of the response. The four poles, $(\pm q_+, \pm q_-)$, of $G_\perp(s)$ are functions, of X and Y (see expression in the Appendix B).

The Green's function allows us to study the phase space of the model, i.e., the shape of the mechanical response u_n as a function of X and Y . The shape phase diagram is shown in Fig. 2, and presents three distinct regions defined as follows. In region \mathcal{A} (shown in green in Fig. 2a) the roots are complex with non-vanishing real and imaginary parts,

$$\mathcal{A}: \quad 0 < Y < \frac{1}{2} \frac{1}{1-X}; \quad Rq_\pm = \omega^{\mathcal{A}} \mp i\lambda^{\mathcal{A}} \quad (28)$$

In this region, deformations oscillate with spatial period (oscillation length) $2\pi R/\omega^{\mathcal{A}}$ and decay over a characteristic decay length $R/\lambda^{\mathcal{A}} > 0$.

The Green's function in the real space reads

$$G_\perp^{\mathcal{A}}(s) = \Upsilon \frac{e^{-\lambda^{\mathcal{A}} \frac{|s|}{R}}}{2} \left[\frac{1}{\lambda^{\mathcal{A}}} \left(1 - \frac{1}{\lambda^{\mathcal{A}2} + \omega^{\mathcal{A}2}} \right) \cos \left(\omega^{\mathcal{A}} \frac{|s|}{R} \right) - \frac{1}{\omega^{\mathcal{A}}} \left(1 + \frac{1}{\lambda^{\mathcal{A}2} + \omega^{\mathcal{A}2}} \right) \sin \left(\omega^{\mathcal{A}} \frac{|s|}{R} \right) \right], \quad (29)$$

where $\Upsilon = \frac{\delta\psi}{4} \frac{1-X^2}{Y(1-X^2)-1} Z$. The tube plotted in region

\mathcal{A} (Fig. 2a) gives an illustration of the shapes obtained in this zone.

For region \mathcal{B} (shown in orange in Fig. 2a) the poles are purely imaginary,

$$\mathcal{B}: \quad \frac{1}{2} \frac{1}{1-X} < Y < \frac{1}{1-X^2}; \quad Rq_\pm = i\lambda_\pm^{\mathcal{B}}, \quad (30)$$

with $\lambda_+^{\mathcal{B}} > \lambda_-^{\mathcal{B}} > 0$, and deformations are associated with two decay lengths $R/\lambda_\pm^{\mathcal{B}}$, according to

$$G_\perp^{\mathcal{B}}(s) = \frac{\Upsilon}{\lambda_+^{\mathcal{B}2} - \lambda_-^{\mathcal{B}2}} \left(\frac{\lambda_+^{\mathcal{B}2} + 1}{\lambda_+^{\mathcal{B}}} e^{-\lambda_+^{\mathcal{B}} \frac{|s|}{R}} - \frac{\lambda_-^{\mathcal{B}2} + 1}{\lambda_-^{\mathcal{B}}} e^{-\lambda_-^{\mathcal{B}} \frac{|s|}{R}} \right). \quad (31)$$

Finally, the region \mathcal{C} (blue in Fig. 2a) is associated with four real poles,

$$\mathcal{C}: \quad \frac{1}{1-X^2} < Y, \quad Rq_\pm = \omega_\pm^{\mathcal{C}} > 0. \quad (32)$$

This region corresponds to a buckling instability zone. Competition between tangential and normal forces in tubular membranes can produce peristaltic shapes which wavelength depends on the system²³. Here, a local perturbation induces a non decaying response that is given by

$$G_\perp^{\mathcal{C}}(s) = \frac{\Upsilon}{\omega_+^{\mathcal{C}2} - \omega_-^{\mathcal{C}2}} \left[\frac{1 - \omega_+^{\mathcal{C}2}}{\omega_+^{\mathcal{C}}} \sin \left(\omega_+^{\mathcal{C}} \frac{|s|}{R} \right) - \frac{1 - \omega_-^{\mathcal{C}2}}{\omega_-^{\mathcal{C}}} \sin \left(\omega_-^{\mathcal{C}} \frac{|s|}{R} \right) \right], \quad (33)$$

which involves two oscillating lengths $2\pi R/\omega_\pm^{\mathcal{C}}$.

The characteristic lengths - the inverses of real and imaginary parts of the poles given above - rescaled by the cylinder radius R , are plotted in Fig. 2b,c as functions of X for two fixed values of Y . When $Y = 0.5$ (Fig. 2c), one sees that for $X < 0$, corresponding to region \mathcal{B} , the two decay lengths $1/\lambda_\pm^{\mathcal{B}}$ (shown in orange

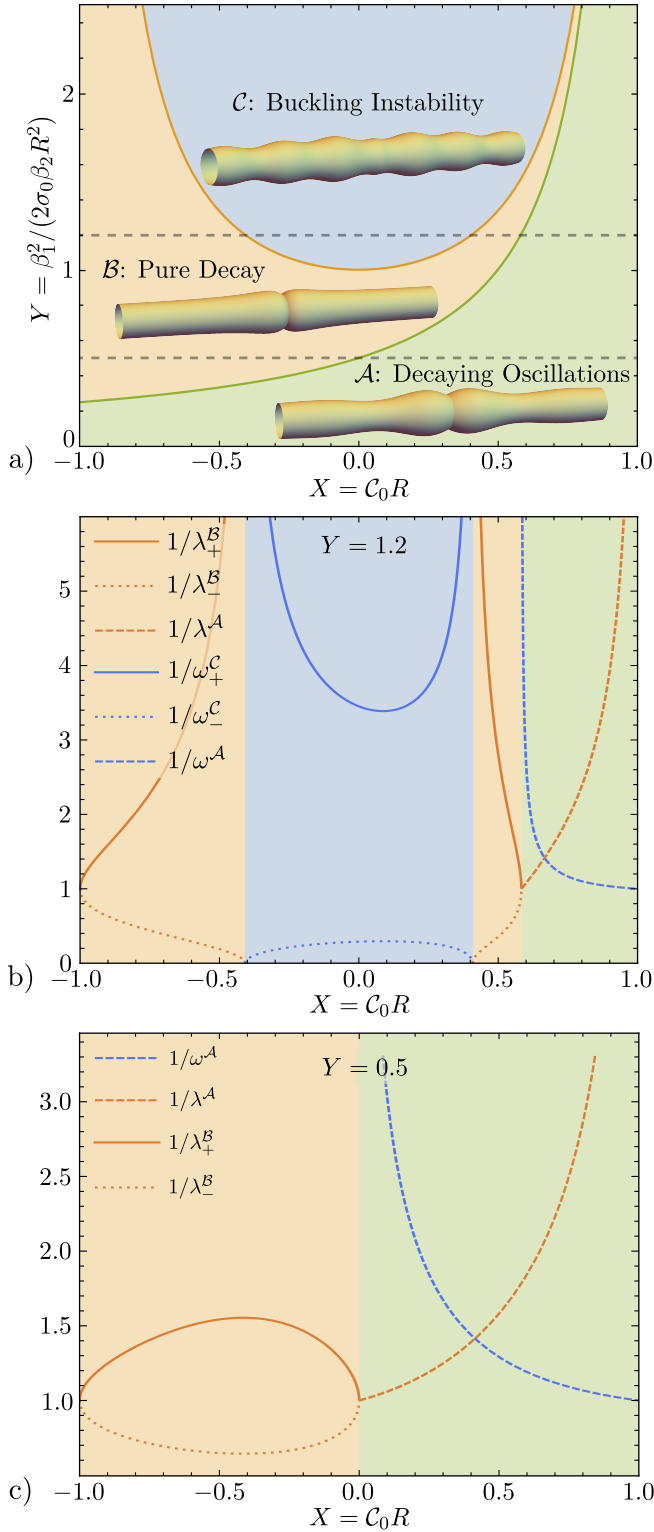


FIG. 2. a) Phase diagram of the deformed cylinder in the (X, Y) plane. Region \mathcal{A} (green): decaying oscillation deformation; region \mathcal{B} (orange), decayig deformation; region \mathcal{C} (blue): buckling instability. Decaying (R/λ) and oscillation (R/ω) lengths as a function of X for (b) $Y = 0.5$ and (c) $Y = 1.2$.

solid and dotted lines) remain finite with $1/\lambda_+^{\mathcal{B}} > 1$ (orange solid line) and $1/\lambda_-^{\mathcal{B}} < 1$ for $-1 < X < 0$, while both take the value of 1 at $X = -1$ (the edge of the valid domain for X) and $X = 0$. For $X > 0$, i.e., in region \mathcal{A} , the oscillation length $1/\omega^{\mathcal{A}}$ (blue dashed line) diverges at $X = 0$ but decreases monotonically with X to reach 1 for $X = 1$. On the contrary, the decay length $1/\lambda^{\mathcal{A}}$ (red dashed line) monotonically increases from 1 for $X = 0$ to diverge in the limit $X \rightarrow 1$, indicative of a buckling instability at $X = 1$. Fig. 2b shows the characteristic lengths as a function of X for $Y = 1.2$. The behavior of the characteristic lengths in regions \mathcal{A} and \mathcal{B} is similar to the one previously described, but a domain pertaining to region \mathcal{C} is intercalated in region \mathcal{B} (at $-0.48 < X < 0.48$), domain in which the oscillation length $1/\omega_+^{\mathcal{C}}$ (blue solid line) reaches a minimum between its two positive diverging limits on the borders between regions \mathcal{B} and \mathcal{C} . Finally, $1/\omega_-^{\mathcal{C}}$ (blue dotted line) vanishes on the borders between regions \mathcal{B} and \mathcal{C} and reaches a maximum in between. The analysis of the Green's functions on the transition lines is presented for completeness in the Appendix C.

To conclude, in this section we have derived the shape equation for an inhomogenous membrane and determined the phase diagram of the model in a cylindrical geometry. We have shown that the coupling of geometry and internal degrees of freedom can generate a rich variety of responses. In the next section, we apply this model to the mitochondrial inner membranes, or cristae.

III. APPLICATION TO THE CRISTAE MEMBRANE

In this section, we use our model to describe the deformation of the mitochondrial cristae induced by a surface pH gradient.

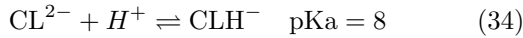
Mitochondria are composed of two membranes, the so-called outer and the inner membrane. While the outer membrane provides the outer envelope of the mitochondrion (as its name suggests), the inner membrane (IM) - enclosing the matrix - contains the protein complexes necessary for energy production. More specifically, the IM forms tubular and “pancake-like” invaginations named cristae that are the place of ATP synthesis from ADP. This endothermic reaction is catalyzed by ATP synthase, a transmembrane protein located in the zones of high curvature of the cristae. ATP synthase uses a gradient of the proton electrochemical potential between the two sides of the IM driving force. Protons in the cristae are supplied by transmembrane proteins of the electron transport chain (also referred to as respiratory chain), which inject protons from the matrix in the cristae. As these proteins are located in flat regions of the cristae, ATP synthase and respiratory chain proteins are spatially separated and the protons diffuse from one site to the other. Notably, the protons are thought to diffuse along the cristae membrane and not in the bulk^{24–26}.

The mechanisms that couple respiratory chain com-

plexes and ATP synthase proteins to ensure efficient ATP synthesis are a very active field of research. Here, we focus on the coupling between a proton gradient and the shape of the cristae membrane which has been observed to change from a regular cylinder to a bumpy irregular tubule when submitted to proton gradients of increasing intensity²⁰.

A. Cristae membrane composition and the importance of cardiolipins

The mitochondrial IM is partly composed of cardiolipin (CL), an anion-acid lipid, found in the majority of membrane organelles that enclose oxidative phosphorylation processes. The value of CL's second pKa, associated with the proton exchange,



suggests that at physiological conditions - pH=7 -, the CL carries a unique charge²⁷.

It has been speculated that this lipid could thus play the role of a proton trap creating a surface proton reservoir independently of the bulk pH in the cristae^{25,27}. Moreover, *in vitro* experiments suggest that the change of the protonation state of CL could affect the membrane mechanical properties¹⁷.

In order to take into account the potential coupling of the CL protonation state (related to the local proton concentration) to the membrane shape, we thus consider the density field ρ and the composition field ϕ introduced in the model (see Eq. (2)) to be given by the densities of the two cardiolipin forms HCL^- and CL^{2-} , such that $\rho(s) = \rho_{\text{CL}^{2-}} + \rho_{\text{HCL}^-}$ and $\phi(s) = \rho_{\text{CL}^{2-}}/\rho$.

In the following, we model the cristae as a membrane tube of length L , that is closed by a spherical cap which we will not further consider here. The reference state corresponds to a homogeneous CL distribution in the absence of catalytic activity of the electron transport chain and ATP synthase, and accordingly $\psi = 0$. We assume that the (cylindrical) reference state is in mechanical equilibrium. Its internal tension is counterbalanced by an external tension \mathbf{f}_{ext} applied at $s = 0, L$. Following Eq. 17, this external force is given by

$$\mathbf{f}_{\text{ext}}(0) = -\mathbf{f}_{\text{ext}}(L) = -\frac{2\sigma_0}{1+X}\mathbf{e}_s. \quad (35)$$

In order to determine the compositional profile $\psi(s)$ of the CLs in the catalytically active state, we first consider the surface concentration gradient of protons along the cristae membrane and then infer the local shift in CL^{2-} and HCL^- concentrations based on the protonation rate constants. The surface concentration profile of protons can be written as $[\text{H}^+] = h_0 + h(s)$. The homogeneous proton concentration h_0 , associated with the reference state, corresponds to the density of protons trapped by the CL in the undeformed cylinder, for which both the

respiratory chain proteins and the ATP synthase do not present catalytic activities. Note that this state is also referred to as state IV of the organelle²⁰. We denote by $h(s)$ the perturbation of the surface proton field due to the catalytic activities of the proteins that inject and consume H^+ . To determine $h(s)$, we model the system as follows (see sketch in Fig. 3a). At one end of the cylinder ($s = 0$), we assume a reflecting barrier for the proton flux, $dh/ds|_{s=0}$, modeling the role of the cristae junction proteins²⁹. At the other end of the cylinder ($s = L$), a ring-shaped proton sink with a spatial extension of Δ_{out} models the proton consumption of ATP synthase proteins. At $s = L_s$, a ring-shape proton source, with a spatial extension of Δ_{in} , models the proton insertion of the respiratory chain. The profile $h(s)$ then satisfies the following stationary diffusion equation,

$$D \frac{\partial^2 h}{\partial s^2}(s, t) + S_{\text{in}}(s) - S_{\text{out}}(s) = 0, \quad (36)$$

where D is the proton diffusion constant and

$$S_{\text{in}}(s) = \frac{k_{\text{in}}}{\sqrt{2\pi\Delta_{\text{in}}^2}} \exp\left(-\frac{1}{2\Delta_{\text{in}}^2}(s - L_s)^2\right) \quad (37)$$

$$S_{\text{out}}(s) = \frac{k_{\text{out}}(h_0 + h(s))}{\sqrt{2\pi\Delta_{\text{out}}^2}} \exp\left(-\frac{1}{2\Delta_{\text{out}}^2}(s - L)^2\right) \quad (38)$$

are the expressions for the source and sink injection and consumption rates, respectively. The numerical values of the parameters introduced here are specified in Table I.

The ratio $h(s)/h_0$ - with $h(s)$ solution of Eq. (36) - is shown in Fig. 3b (blue line). The proton concentration profile indicates an excess of protons in the zone of the respiratory chain (modeled by the proton source) and a lack of protons in the zone of ATP synthase enrichment (modeled by the proton sink), in agreement with *in vivo* pH measurements³⁰.

The inhomogeneity in the proton profile will induce an inhomogeneity in the lipid composition due to a shift in the chemical equilibrium between the two forms of CL. In the reference state, the lipid composition is $\phi_0 = \rho_{\text{CL}^{2-},0}/\rho_0$. Using the conservation of matter, the variation in the composition can be expressed to the first order in h as

$$\psi(s) = -(1 - \phi_0) \frac{h(s)}{h_0}. \quad (39)$$

See Appendix D for details. The profile $\psi(s)$ for an initial $\phi_0 = 0.5$ is plotted in Fig. 3b (red line). As expected, one can observe an enrichment in protonated CLs (corresponding to $\psi < 0$) close to the proton source and in deprotonated CLs close to the proton sink.

B. Mitochondrial cristae shape in the presence of catalytic activity

Based on our simple model of a CL composition gradient in the cristae membrane, we now solve the shape

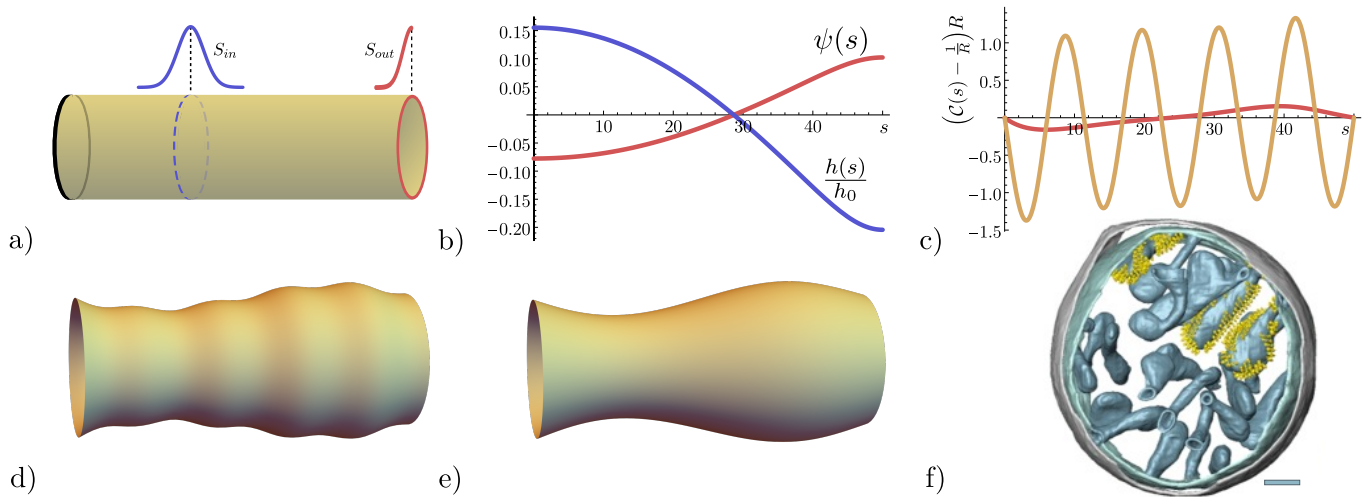


FIG. 3. a) Finite cylinder of length L on which is included a surface source S_{in} and sink S_{out} of protons. b) Proton profile $h(s)/h_0$ and consequent lipid composition $\psi(s)$. Solutions of Eqs. (36, 39) for parameters given in Tab. (I). c) Contribution to the density inhomogeneity proportional to the curvature $(\mathcal{C} - \mathcal{C}_{eq})$ (plot red corresponds to shape e) plot orange to shape d). d) Example of a solution of Eq. (25) for $h_0 = 30$ protons.nm $^{-1}$, $\phi_0 = 0.5$, $X = 0.21$, $Y = 1.1$ and $Z = 17$. e) Example of a solution for the same parameters as d) except for $X = -0.25$, $Y = 0.5$, $Z = 40$. f) Reproduction of a graphical scheme of a Cryo-ET of isolated *Polytomella* sp. mitochondria, scale bar 100nm.²⁸

equation Eq. (25) given the inhomogeneous field $\psi(s)$ and assuming that the mechanical boundary conditions remain unchanged, i.e., we still consider a pinned protrusion with fixed (reference state) curvature in $s = 0$ and $s = L$.

The latter leads to the following conditions on the radial deformation field:

$$\begin{aligned} u_n(0) &= 0, & u_n(L) &= 0 \\ u_r''(0) &= 0, & u_r''(L) &= 0. \end{aligned} \quad (40)$$

The solutions to the shape equation subject to these boundary conditions were obtained by numerical integration.

In Fig. 3d,e, we show the membrane shapes obtained for two sets of parameters, one belonging to region \mathcal{B} of the shape phase diagram (Fig. 3e) and one to region \mathcal{C} (Fig. 3d). Both present a bulge close to the proton sink and a narrow bottleneck around the proton source. For the parameters belonging to region \mathcal{B} (Fig. 3e), the overall shape is smooth, whereas for parameters of region \mathcal{C} (Fig. 3d), the shape presents a succession of oscillations modulating the major bulge and narrow, signature of the buckling instability observed in this region. In general, the shapes are in qualitative agreement with recent electron microscopy observations. A Cryo-ET image of mitochondria is reproduced from²⁸ in Fig. 3f and one can identify the necks and bulges in cristae. Finally, we consider the density inhomogeneity $r(s)$ induced by the composition perturbation $\psi(s)$. The expression given in Eq. (9) shows that $r(s)$ is the sum of a term proportional to ψ and a term involving the curvature. When the coupling between r and ψ dominates, quantified by the value of σ_1 , the inhomogeneity in mass density follows ψ . When

the coupling between r and the curvature is dominant, quantified by the value of β_1 and consequently Y , the inhomogeneity in the density will be given by the variation of the curvature $(\mathcal{C} - \mathcal{C}_{eq})$. This contribution is plotted in Fig 3c for the two shapes we have considered above and shown in Fig. 3d,e. One retrieves the unique narrow and bulge of the shape shown in Fig 3e (red line in Fig 3c) and a succession of dense and sparse zones remindful of the shape shown in Fig 3d (orange line in Fig 3c).

IV. CONCLUSION

In this work, we first presented a generalized Helfrich model for inhomogeneous membranes with a coupling between membrane geometry and internal degrees of freedom related to membrane composition. We showed that the shape of such systems can easily be studied after derivation of the stress tensor obtained via a constrained minimization of the Hamiltonian. We show that, in the case of cylindrical geometries, these systems present a rich phase diagram and could explain deformations observed both for *in vitro* and *in vivo* systems. This model could be applied to CL membranes that are known to deform under pH variation¹⁷. Recently, controlled microfluidic devices were developed to monitor the vesicles response to a variation of chemical environment (salt concentration or pH)^{16,32}. Such protocols could be used to validate and parametrize the model.

We then applied this framework, combined with a simple model of proton transport at the cristae surface, to describe the shape deformations of mitochondrial cristae driven by the surface proton flux established between

L	50 nm	k_{in}	$6 \cdot 10^6 \text{ s}^{-130}$
R	10 nm	k_{out}	$3.24 \cdot 10^5 \text{ proton}^{-1} \text{ s}^{-130}$
L_s	9.5 nm	D	$10^7 \text{ nm}^2 \text{ s}^{-126}$
Δ_{in}	20 nm	Δ_{out}	5 nm
κ	10^{-10} N nm	σ_0	$10^{-16} \text{ N nm}^{-131}$

TABLE I. Values of the model parameters.

proton sources and sinks, and that arise as a consequence of inhomogeneities in the membrane composition downstream of the proton concentration gradient. Our model reproduces the characteristic alternation between more constricted and wider regions typically associated with spatially varying rates of ATP synthesis in the cristae²⁸.

Acknowledgments H.B. thanks A.-F. Bitbol, J. Heberle, S. Bloch and R. Netz for useful discussions. H.B. acknowledges funding from Humboldt Research Fellowship Program for Experienced Researchers.

V. APPENDIX

A. Elements of differential geometry for a deformed cylinder

We use a standard parametrization for axisymmetric surfaces, s is the arclength, θ the revolution angle. $\mathbf{X}(\theta, s)$ gives the cylindrical surface and the deformation components are $\delta\mathbf{X} = \mathbf{u}$. We assume no deformations on the θ direction. Thus it gives:

$$\mathbf{X} = \begin{pmatrix} R \cos \theta \\ R \sin \theta \\ s \end{pmatrix}, \quad \delta\mathbf{X} = \begin{pmatrix} u_n(s) \cos \theta \\ u_n(s) \sin \theta \\ u_s(s) \end{pmatrix} \quad (41)$$

where $\theta \in [0, 2\pi[$ and $s \in [0, L]$, these are the curvilinear coordinates on the surface of the undeformed cylinder of radius R (see Figure 1). The intrinsic basis is given by:

$$\begin{aligned} \mathbf{e}_1 = \mathbf{e}_\theta &= \begin{pmatrix} -(R + u_n) \sin \theta \\ (R + u_n) \cos \theta \\ 0 \end{pmatrix}, \\ \mathbf{e}_2 = \mathbf{e}_s &= \begin{pmatrix} u'_n \cos \theta \\ u'_n \sin \theta \\ 1 + u'_s \end{pmatrix}, \\ \mathbf{n} &= \begin{pmatrix} \cos \theta \\ \sin \theta \\ -u'_n \end{pmatrix}. \end{aligned} \quad (42)$$

where we use $s_1 = \theta$ and $s_2 = s$ such that the normal vector points to the outside of the tube and the prime means derivative with respect to s . The metric g_{ab} and the curvature K_{ab} are expressed to the first order in the deformation field

$$g_{ab} = \begin{pmatrix} R^2 + 2Ru_n & 0 \\ 0 & 1 + 2u'_s \end{pmatrix}, \quad K_{ab} = \begin{pmatrix} R + u_n & 0 \\ 0 & -u''_n \end{pmatrix}, \quad (43)$$

where a and b are equal to 1 or 2. With this parameterization of our system the area element is given by:

$$dA = (R + u_n + Ru'_s) d\theta ds. \quad (44)$$

Moreover, the normal and scalar curvatures are given by:

$$\mathcal{C} = \frac{1}{R} - \left(\frac{u_n}{R^2} + u''_n \right), \quad \mathcal{R} = -2 \frac{u''_n}{R}, \quad (45)$$

and the Christoffel symbols are

$$\Gamma_{ab}^\theta = \begin{pmatrix} 0 & u'_n/R \\ u'_n/R & 0 \end{pmatrix}, \quad \Gamma_{ab}^s = \begin{pmatrix} -Ru'_n & 0 \\ 0 & u''_s \end{pmatrix}. \quad (46)$$

B. Roots of Green's function

We give here the general expressions of the four poles ($\pm Rq_\pm$) of the Green's function:

$$R^2 q_\pm^2 = \frac{Y(1 - X^2) - X}{Y(1 - X^2) - 1} \pm \frac{\sqrt{(Y(1 - X^2) - X)^2 - (Y(1 - X^2) - 1)^2}}{Y(1 - X^2) - 1}. \quad (47)$$

C. Green's function on line \mathcal{A}/\mathcal{B} and \mathcal{B}/\mathcal{C}

The line separating the regions \mathcal{A} and \mathcal{B} , of equation $Y = 1/(2(1-X))$, is associated with the Green's function,

$$G_{\perp}^{\mathcal{A}/\mathcal{B}}(s) = \frac{\delta\psi Z}{2R}(1+X)|s|e^{-|s|/R} \quad (48)$$

The line separating the decay oscillating shapes, in region \mathcal{B} and the buckling region \mathcal{C} , is associated with an unphysical long-range Green's function written as,

$$G_{\perp}^{\mathcal{B}/\mathcal{C}}(s) = -\frac{\delta\psi RZ}{4}(1+X)\left(\delta(s) + \frac{|s|}{2R^2}\right) \quad (49)$$

This behavior is due to the simultaneous cancellation of the prefactor of the q^4 term of the Green's function denominator (effective bending constant) and of the constant term of the Green's function.

D. Derivation of the composition expression, Eq. (39)

Consider the protonation of CL^{2-} , Eq. (34), in the reference (undeformed) cylinder:

$$\phi_0 = \frac{[CL^{2-}]_0}{[HCL^-]_0 + [CL^{2-}]_0} = \frac{R}{1-R}, \quad (50)$$

with $R = \frac{[CL^{2-}]_0}{[HCL^-]_0}$. Using the equilibrium condition from pKa we have

$$K_a = h_0 \frac{[CL^{2-}]_0}{[HCL^-]_0} = \frac{h_0\phi_0}{1-\phi_0}. \quad (51)$$

Applying the previous condition to the deformed state (up to first order) one obtains

$$\psi(s) = -(1-\phi_0)\frac{h(s)}{h_0}. \quad (52)$$

¹P. Brzezinski, M. Bränden, T. Sanden and J. Widegren. Localized proton microcircuits at the biological membrane–water interface. *Proc. Natl. Acad. of Sci. USA*, 103:19766–19770, 2006.

²W. Helfrich. Elastic properties of lipid bilayers—theory and possible experiments. *Z. Naturforsch.*, 33:305–315, 1973.

³U. Seifert. Configurations of fluid membranes and vesicles. *Advances in Physics*, 46(1):13–137, 1997.

⁴U. Seifert and R. Lipowsky. *Handbook of Biological Physics*. Elsevier Science.

⁵A.-F. Bitbol, L. Peliti and J.-B. Fournier. Membrane stress tensor in the presence of lipid density and composition inhomogeneities. *EPJE*, 34(5):53, 2011.

⁶T. C. Lubensky and J. Prost. Orientational order and vesicle shape. *J. Phys. II France*, 2:371–382, 1992.

⁷M. Hamm and M.M. Kozlov. Elastic energy of tilt and bending of fluid membranes. *EPJE*, 3:323–335, 2000.

⁸Ou-Yang Zhong-can and W. Helfrich. Bending energy of vesicle membranes: General expressions for the first, second and third variation of the shape energy and applications to spheres and cylinder. *Phys. Rev. A*, 39(10):5280–5288, 1989.

⁹R. Capovilla and J. Guven. Stresses in lipid membranes. *Journal of Physics A: Mathematical and General*, 35(30):6233, 2002.

¹⁰R. Capovilla and J. Guven. Stresses in lipid membranes. *J. Phys. A*, 35(30):6233–6247, 2002.

¹¹J. Guven. Membrane geometry with auxiliary variables and quadratic constraints. *Journal of Physics A: Mathematical and General*, 37(28):L313, 2004.

¹²M. Deserno. Fluid lipid membranes: From differential geometry to curvature stresses. *Chemistry and physics of lipids*, 185:11–45, 2015.

¹³H. Berthoumieux, J.-L. Maître, C.-P. Heisenberg, E. K. Paluch, F. Jülicher and G. Salbreux. Active elastic thin shell theory for cellular deformations. *New Journal of Physics*, 16:065005, 2014.

¹⁴G. Salbreux and F. Jülicher. Mechanics of active surfaces. *Phys. Rev. E*, 96(3):032404, 2017.

¹⁵A. Mietke, F. Jülicher and I. F. Sbalzarini. Self-organized shape dynamics of active surfaces. *Proc. Natl. Acad. of Sci. USA*, 116(1):29–34, 2019.

¹⁶D. Roy R. Dasgupta R. Lipowsky M. Karimi, J. Steinkühler and R. Dimova. Asymmetric ionic conditions generate large membrane curvatures. *NanoLetters*, 18:7816–7821, 2018.

¹⁷N. Khalifat, N. Puff, S. Bonneau, J.-B. Fournier and M. I. Angelova. Membrane deformation under local pH gradient: mimicking mitochondrial cristae dynamics. *Biophys. J.*, 95(10):4924–4933, 2008.

¹⁸K. G. Hugentobler, D. Heinrich, J. Berg, J. Heberle, P. Brzezinski, R. Schlesinger and S. Block. Lipid composition affects the efficiency in the functional reconstitution of the cytochrome c oxidase. *IJMS*, 21:6981, 2020.

¹⁹F. Joubert and N. Puff. Mitochondrial cristae architecture and functions: lessons from minimal model systems. *Membranes*, 11(465):11070465, 2021.

²⁰C. A. Mannella. Structure and dynamics of the mitochondrial inner membrane cristae. *Biochimica et Biophysica Acta (BBA)-Molecular Cell Research*, 1763(5-6):542–548, 2006.

²¹S. Cogliati, J. Enriquez and L. Scorrano. Mitochondrial cristae: where beauty meets functionality. *Trends in Biochemical Sciences*, 41(3):261–273, 2016.

²²N. Patil, S. Bonneau, A.-F. Bitbol F. Joubert and H. Berthoumieux. Mitochondrial cristae modeled as an out-of-equilibrium membrane driven by a proton field. *Phys. Rev. E*, 102(11):022401, 2020.

²³R. Bar-Ziv and E. Moses. Instability and "pearling" states produced in tubular membranes by competition of curvature and tension. *Phys. Rev. Lett.*, 73:1392–1395, 1994.

²⁴J. Heberle, J. Riesle, G. Thiedemann, D. Oesterheld, and N. A. Dencher. Proton migration along the membrane surface and retarded surface to bulk transfer. *Nature*, 370:379–382, 1994.

²⁵J. Heberle. Proton transfer reactions across bacteriorhodopsin and along the membrane. *BBA-Bioenergetics*, 1458:135–147, 2000.

²⁶R. B. Gennis. Proton dynamics at the membrane surface. *Bio-phys. J.*, 110(1909-19011).

²⁷N. A. Dencher T. H. Haines. Cardiolipin: a proton trap for oxidative phosphorylation. *FEBS*, 528:35–39, 2002.

²⁸T. Meier K. M. Davies W. Kühlbrandt T. B. Blum and A. Hahn. Dimers of mitochondrial atp synthase induce membrane curvature and self-assemble into rows. *Proc. Natl. Acad. Soc. USA*, 116:4250–4255, 2019.

²⁹N. Pfanner, M. van der Laan and S. E. Horvath. Mitochondrial contact site and cristae organizing system. *Current Opinion in Cell Biology*, 41:33–42, 2016.

³⁰B. Rieger, W. Junge, and K. B Busch. Lateral pH gradient between oxphos complex iv and f0f1 atp-synthase in folded mitochondrial membranes. *Nat. Commun.*, 5:3103, 2014.

³¹A.-F. Bitbol, N. Puff, J.-B. Fournier Y. Sakuma, M. Imai and M. I. Angelova. Lipid membrane deformation in response to a local pH modification: theory and experiments. *Soft Matter*, 8:6073–6082, 2012.

³²S. Pramanik, J. Steinküler, R. Dimova, J. Spatz and R. Lipowsky.
Binding of his-tagged fluorophores to lipid bilayers of giant vesi-

cles. *Soft Matter*, 34:6372, 2022.